

Non-isothermal Reduction Kinetics of Iron During Vacuum Carbothermal Reduction of Ilmenite Concentrate



HUANG RUN, LV XIAODONG, WU QINGHUI, WU QINZHI, and ZHANG JINZHU

The non-isothermal reduction kinetics and mechanism of iron during vacuum carbothermal reduction of ilmenite concentrate were investigated by X-ray diffraction, backscattered electron imaging, and energy-dispersive X-ray spectroscopy at temperatures from 1273 K to 1673 K (1000 °C to 1400 °C). The pressure dropped and the increasing trend of mass loss and metallization ratios slowed down when the temperature was higher than 1573 K (1300 °C). The reaction products were iron, Ti_2O_3 , and silicate. Iron was mainly obtained by carbothermal reduction of $FeTiO_3$ and $FeTi_2O_5$. The irons continued to nucleate, aggregate, and grow during the reduction process. Comprehensive consideration of Šatava–Šesták method and Coats–Redfern method, the apparent activation energy of the reduction process was 587.4 ± 2.98 kJ/mol, and the forms of both integral and differential for the mechanism function were $G(a) = [(1-a)^{-1/3} - 1]^2$ and $f(a) = 3/2(1-a)^{4/3}[(1-a)^{-1/3} - 1]^{-1}$, respectively.

<https://doi.org/10.1007/s11663-019-01529-9>

© The Minerals, Metals & Materials Society and ASM International 2019

I. INTRODUCTION

THE most important primary minerals of titanium are rutile and ilmenite. Only rutile and ilmenite are suitable for titanium production and titanium white industry at present.^[1] The utilization of low-grade minerals, such as ilmenite, has attracted increasing attention considering the worldwide decrease in sources of high-grade titanium mineral. Over 90 pct of titanium resources of China are located in Panxi, which account for 35 pct of the world reserves. However, they are mainly complex symbiotic ores.^[2] Panzhihua ilmenite concentrate is re-beneficiated from tailing after the first beneficiation. The content of TiO_2 is in the range 45.5 to 48.5 pct, that of iron is 30.0 to 33.5 pct, and that of non-ferrous impurities is 11.0 to 12.0 pct.^[3] The production process of Ti-rich materials is mainly divided into hydrometallurgy and pyrometallurgy. Hydrometallurgy mainly includes direct acid leaching^[4,5] and reduction rust,^[6] and the pyrometallurgy mainly includes electric smelting^[7] and selective chlorination.^[8] In the experiments of Lv *et al.*,^[9] an economical and clean method for semi-molten reduction followed by magnetic separation to produce titanium slag from

Panzhihua ilmenite concentrate was presented. In study of Zhang *et al.*,^[10] a new process named vacuum separation was found to produce high-grade TiO_2 materials. The smelting of titanium slag by electric furnace has become the main technical means for preparing titanium-rich materials from ilmenite because of the research situation and the properties of raw materials. Nevertheless, the removal of non-ferrous impurities (Mg, Ca) cannot be achieved, which can influence the production of sponge titanium or titanium white by chlorination.

The effective separation of slag and iron in the process of smelting titanium slag in electric furnace is the key, and the selective reduction of ilmenite is the basis. Many studies have been conducted on the mechanism and kinetics of the reduction of different ilmenites in recent years. Dewan *et al.*^[11] studied the process of carbothermal reduction of ilmenite and considered that the reduction process could be divided into two main stages: $FeTiO_3$ was reduced to Fe and TiO_2 and TiO_2 to TiC_xO_y . Li *et al.*^[12] investigated the reduction process of Panzhihua ilmenite and found that the reduction and decomposition of ilmenite mainly occurred below 1273 K (1000 °C). Fe_3O_4 continued to transform to metal iron, and TiO_2 was reduced to Ti_3O_5 with increasing temperature. Welham *et al.*^[13] observed that ilmenite was rapidly reduced to Fe and TiO_2 , and then TiO_2 was reduced to a series of low-valence oxide Ti_nO_{2n-1} . Ti_3O_5 was finally formed. The existence of Fe was considered to be beneficial to the reduction of Ti_3O_5 . Gou *et al.*^[14] conducted an experiment on the carbothermal reduction process of ilmenite in argon atmosphere and concluded

HUANG RUN, LV XIAODONG, WU QINGHUI, WU QINZHI, and ZHANG JINZHU are with the School of Materials and Metallurgy, GuiZhou University, Guiyang 550000, China. Contact e-mail: jzhang@gzu.edu.cn

Manuscript submitted July 5, 2018.

Article published online February 6, 2019.

that part of carbon dissolved in iron to form a liquid phase when the reaction temperature was higher than 1427 K (1154 °C) of the Fe–C binary system eutectic temperature. The carbon could be transported through liquid iron to the reaction interface. The reduction of ilmenite conformed to the shrinking core model when the reaction temperature was higher than 1573 K (1300 °C). Lv *et al.*^[15] studied the carbothermic reduction behavior of original ilmenite and pre-oxidized ilmenite concentrates and found that the average activation energy of the pre-oxidized ilmenite concentrate was less than that of the original form by approximately 25 pct. Wang *et al.*^[16] studied the kinetics of reduction between natural ilmenite and carbon. Chemical reaction was the rate-controlling step at temperatures below 1373 K (1100 °C), mixed controlling at 1373 K to 1523 K (1100 °C to 1250 °C), and diffusion through the product layer above 1523 K (1250 °C). The activation energies of the three steps were 265, 164, and 157 kJ/mol. In the experiments of Guindy *et al.*,^[17] gas diffusion was the rate-controlling step at 1348 K to 1413 K (1075 °C to 1140 °C), and the activation energy for the reaction was 268 kJ/mol.

The introduction of vacuum metallurgy has solved many problems that are difficult to solve under atmospheric pressure, which can promote the gasification, evaporation, decomposition, and reduction of metal compounds and the degassing of molten metal, thereby reducing the reaction temperature.^[18] The removal of non-iron impurity is realized. In combination with theoretical and experimental studies, Huang *et al.*^[19–21] proposed a new process for preparing high-grade titanium slag by vacuum carbothermic reduction of ilmenite concentrate. When the temperature was above 1773 K (1500 °C) and the carbon content was higher than 12 pct, a high-grade titanium slag (93 pct TiO₂, CaO + MgO < 0.45 pct) was obtained, and effectively removed impurities such as calcium and magnesium. However, the reduction mechanism and kinetics of vacuum reduction process in this process need further investigation. At present, for the research of non-isothermal method, many methods (Kissinger–Akahira–Sunose (KAS), Flynn–Wall–Ozawa (FWO) methods, Šatava–Šesták method, Starink method, Coats–Redfern method, *etc.*)^[22–26] were used to verify each other to find out the kinetic parameters and kinetic

equations. This method can obtain more reliable mechanism functions and kinetic parameters. Therefore, the reduction kinetics of iron in the new process of preparing high-grade titanium slag from vacuum carbothermic reduction ilmenite concentrate was studied by means of mutual verification of Šatava–Šesták method and Coats–Redfern method, and the reduction mechanism and kinetic parameters of the reduction process were proved. It provided a theoretical basis for the separation of slag and iron in the new process of preparing high-grade titanium slag by vacuum carbothermic reduction of ilmenite concentrate.

II. EXPERIMENTAL

A. Materials and Apparatus

The raw material contained ilmenite concentrate and dried coke. The chemical composition of the raw material is shown in Table I, and the X-ray diffraction (XRD) diagram of ilmenite concentrate is depicted in Figure 1, which indicates that Fe mainly existed in ilmenite form, in addition to a small amount of Fe₃O₄. The particle sizes of ilmenite and coke reductant were smaller than 75 μm. The laboratory equipment was an MTLQ-TG-40 vacuum carbon tube furnace.

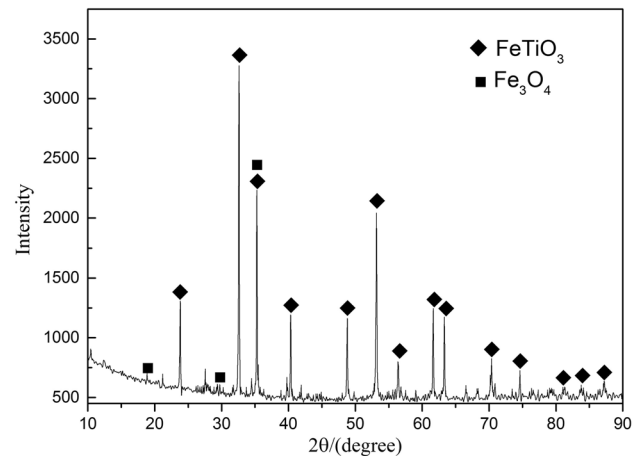


Fig. 1—XRD diagram of ilmenite concentrate.

Table I. Chemical Composition of the Raw Material (Weight Percent)

Ilmenite									
TiO ₂	FeO	Fe ₂ O ₃	CaO	MnO	MgO	SiO ₂	Al ₂ O ₃	V ₂ O ₅	
45.64	36.45	6.53	1.12	0.86	3.22	3.65	1.02	< 0.10	
Coke									
					Ash				
S	P	FC	Volatile	Ash	Fe ₂ O ₃	CaO	Al ₂ O ₃	MgO	SiO ₂
0.65	0.12	83.66	2.22	14.12	8.91	6.01	22.26	2.16	47.79

B. Experimental Procedure

The coke dosage used in the reduction experiments was chosen the carbon-oxygen molar ratio 1:2 on the basis of a previous study.^[27] The agglomerant was methyl cellulose. The ilmenite concentrate, coke, agglomerant, and water were thoroughly mixed and made into pellets under the pressure of 15 MPa. A single specimen was approximately 24.07 g, with a diameter of 30 mm and a height of 13 mm. The specimen was dried at 105 °C for 120 min. The reduction experiments were performed in a vacuum vertical tube furnace equipped with a graphite heater, as schematically shown in Figure 2.

The heating rate was 6 °C/min, heating was stopped immediately when certain setting temperature was finally reached, then the power was cut off, and specimen was cooled to a room temperature through the water cycle. The cooling rates were 13.3 °C/min when the temperature was higher than 1000 °C, 6.15 °C/min when the temperature was from 600 to 1000 °C, and 3 °C/min below 600 °C. The setting temperatures were 1273 K, 1323 K, 1373 K, 1423 K, 1473 K, 1523 K, 1573 K, 1623 K, and 1673 K (1000 °C, 1050 °C, 1100 °C, 1150 °C, 1200 °C, 1250 °C, 1300 °C, 1350 °C, and 1400 °C). The specimen was removed and weighed after cooling to room temperature, and the pellet in each experiment was cut into two pieces. One was used for the chemical analysis of total iron and metallic iron (MFe),^[28] and the other was used for optical microscopy, backscattered electron scanning electron microscopy, energy-dispersive X-ray spectroscopy (EDS), and XRD analysis. The metallization ratio and weight loss ratio were defined as follows:

$$\text{Metallization ratio} = m_{MFe}/m_{TFe} \times 100 \text{ Pct},$$

where m_{MFe} is mass of metal iron in reduced samples and m_{TFe} is the mass of total iron in reduced samples.

$$\text{Mass loss ratio} = (m_0 - m_1 - m_2)/(m_0 - m_2) \times 100 \text{ Pct},$$

where m_0 is the mass of unreduced materials, m_1 is the mass of sample materials after reduction at any temperature, and m_2 is the mass of agglomerant.

III. RESULTS

A. Effect of Temperature on Reduction of Sample

The effect of temperature on metallization ratio, mass loss ratio, and vacuum furnace pressure is shown in Figure 3. The gas produced by the reduction reaction would cause the change of the pressure in the furnace. The mass loss ratio, metallization ratio, and vacuum furnace pressure increased with increase in temperature in a similar trend in the temperature range of 1273 K to 1573 K (1000 °C to 1300 °C), and the increase became faster above 1423 K (1150 °C). When the temperature was higher than 1573 K (1300 °C), the pressure decreased, the increasing trend of metallization ratio slowed down, and the increasing trend of mass loss ratio slowed down but was larger than that of metallization ratio. Therefore, the iron reduction was close to completion, and the titanium oxide continued to deoxidize. At 1673 K (1400 °C), the metallization ratio reached up to 94.3 pct, and the mass loss ratio reached up to 24.1 pct.

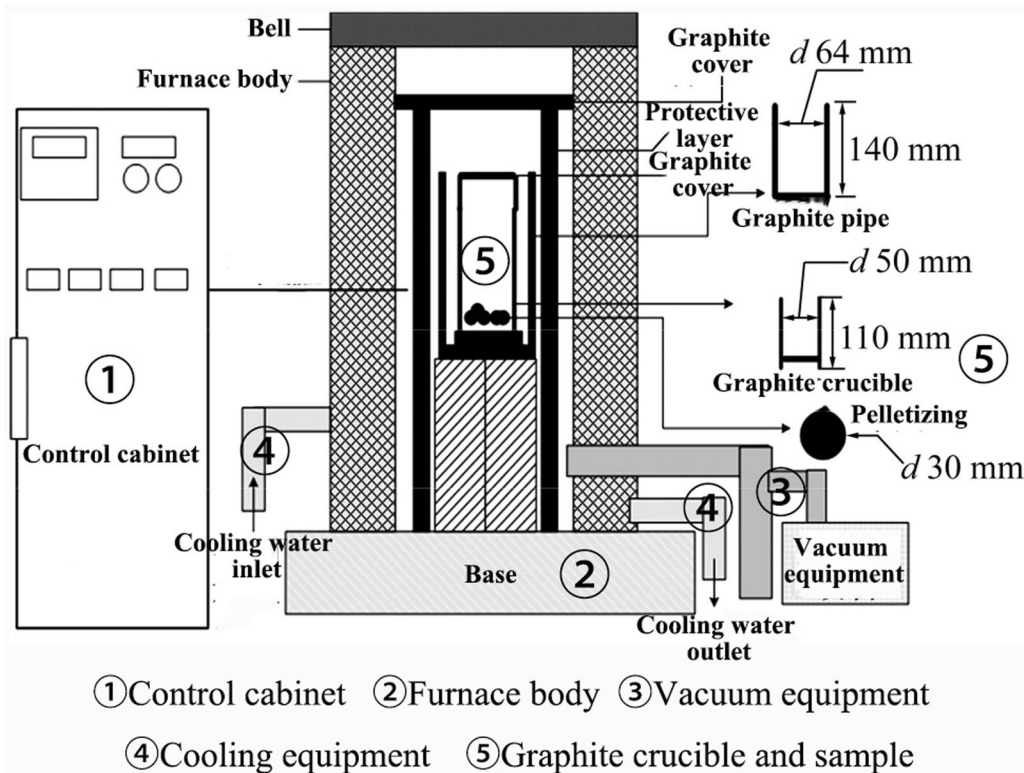


Fig. 2—Schematic diagram of vacuum carbon tube furnace.

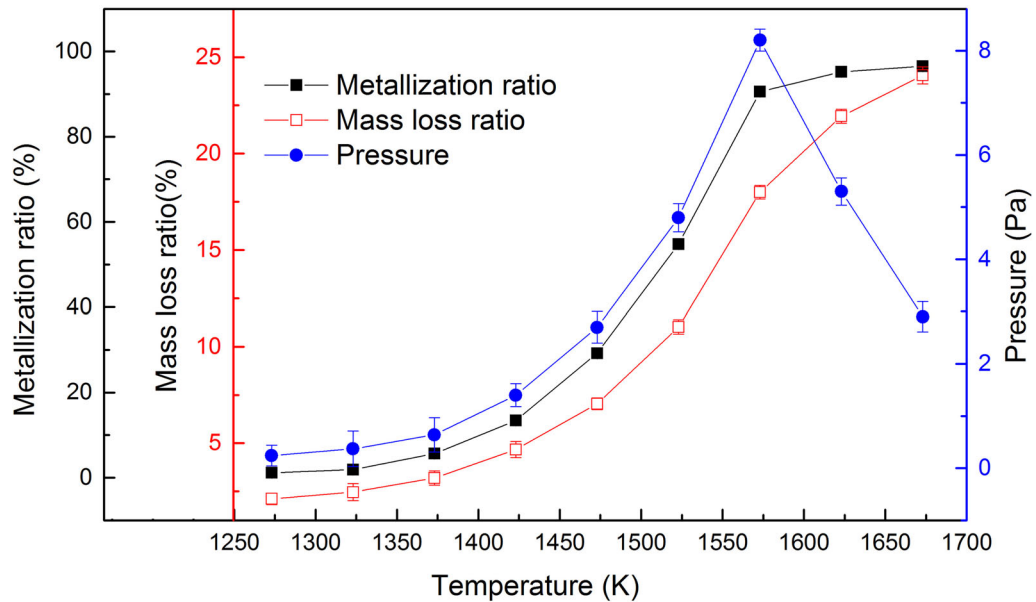


Fig. 3—Effect of temperature on metallization ratio, mass loss ratio, and pressure.

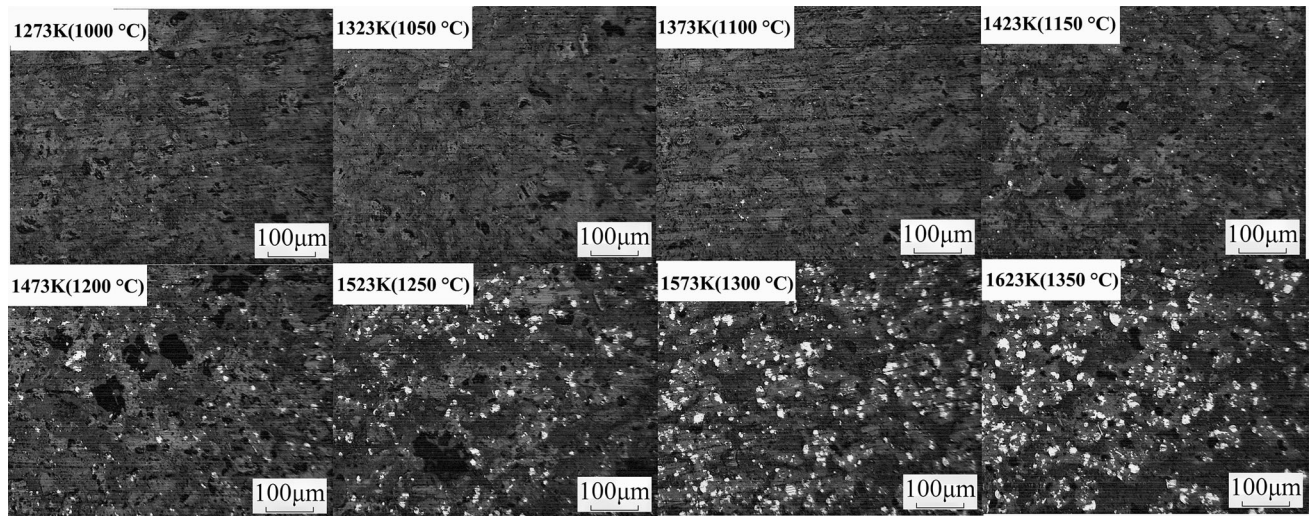


Fig. 4—Mineralogical pictures of the samples reduced with different temperatures.

B. Growth of the Metal Phase of Reduced Samples

The mineralogical pictures of the samples reduced with different temperatures are shown in Figure 4. The white region is MFe. Only a small amount of white region was distributed sporadically at 1273 K to 1423 K (1000 °C to 1150 °C). The white region increased and tended to gather and grow with the increase in temperature when the temperature was higher than 1423 K (1150 °C), which clearly indicated that the iron particle size increased with increasing temperature.

More than 10 continuous pictures of each sample were taken with an optical microscope to obtain an average iron particle size in the reduced sample. The observation areas were randomly distributed in the top,

left, middle, right, and bottom of a sample section. The particle size was automatically analyzed using Image J 1.41 software, and an average value was taken from the results of these pictures. The average size of iron in the reduced samples is shown in Figure 5. The average size of iron almost did not change before 1373 K (1100 °C), and began to increase slowly at 1373 K to 1423 K (1100 °C to 1150 °C); it shown that only a small amount of iron was reduced. The average size of iron increased sharply with the increasing temperature when the temperature was higher than 1423 K (1150 °C), which showed that a great quantity of iron was reduced. The average size of iron gathered and increased with the increase in reduction temperature.

IV. DISCUSSION

A. Analysis of Reduction Process of Iron

The morphology and element distribution of the samples reduced with different temperatures are shown in Figure 6. EDS analysis in more than six locations was performed in the areas represented by *a*, *b*, *c*, and *d* in Figure 6. The average of the atomic percentages of their elements was obtained. The average atomic percentages of elements represented by *a*, *b*, and *c* are shown in

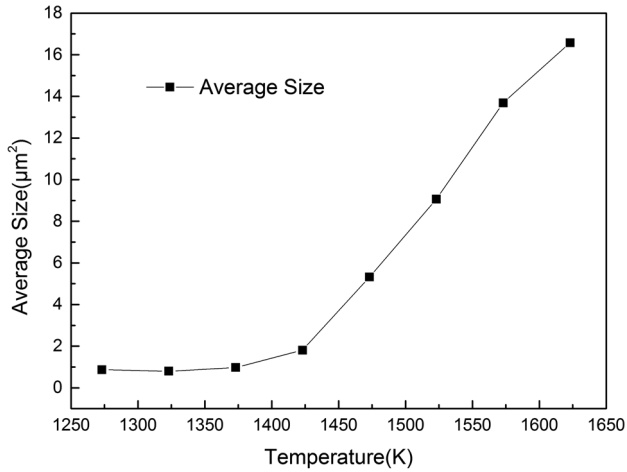


Fig. 5—Average size of iron in the reduced samples with different temperatures.

Tables II and III. Table II and Figures 3 and 6 indicate that the areas were chaotic and minimal iron was reduced at 1323 K to 1423 K (1050 °C to 1150 °C). The areas became smooth and a small amount of iron was reduced at 1473 K (1200 °C). The areas represented by *b* appeared and a great quantity of iron was reduced at 1523 K (1250 °C). The areas represented by *a* disappeared and only a small amount of unreduced iron was distributed in the areas of *b* at 1573 K (1300 °C); the iron reduction was basically completed and only minimal unreduced iron was distributed in the areas of *b* at 1623 K (1350 °C). Figure 6 depicts that the metal iron phase agglomerated and grew at the rear edge represented by *a* and *b* during the reduction.

The XRD results of the reduced samples in different temperatures based on the foregoing results in Tables II and III are given in Figure 7 and Table IV. As the reduction temperature increased, the Fe phase peak gradually increased, and it then rapidly increased at 1473 K to 1523 K (1200 °C to 1250 °C). The phase peak of Fe₂TiO₄ appeared at 1323 K to 1423 K (1050 °C to 1150 °C), which was similar to the study result generated by Fu *et al.*,^[29,30] but the phase peak of other phases still existed. At 1473 K (1200 °C), the phase peak of Fe₂TiO₄ disappeared, the phase peaks of FeTiO₃ and (Fe, Mg)TiO₃ weakened, and the phase peak of FeTi₂O₅ appeared. At 1523 K (1250 °C), the phase peaks of FeTiO₃ and (Fe, Mg)TiO₃ continued to weaken, and the phase peak of FeTi₂O₅ increased suddenly. At 1573 K (1300 °C), the phase peaks of FeTiO₃ and FeTiO₃

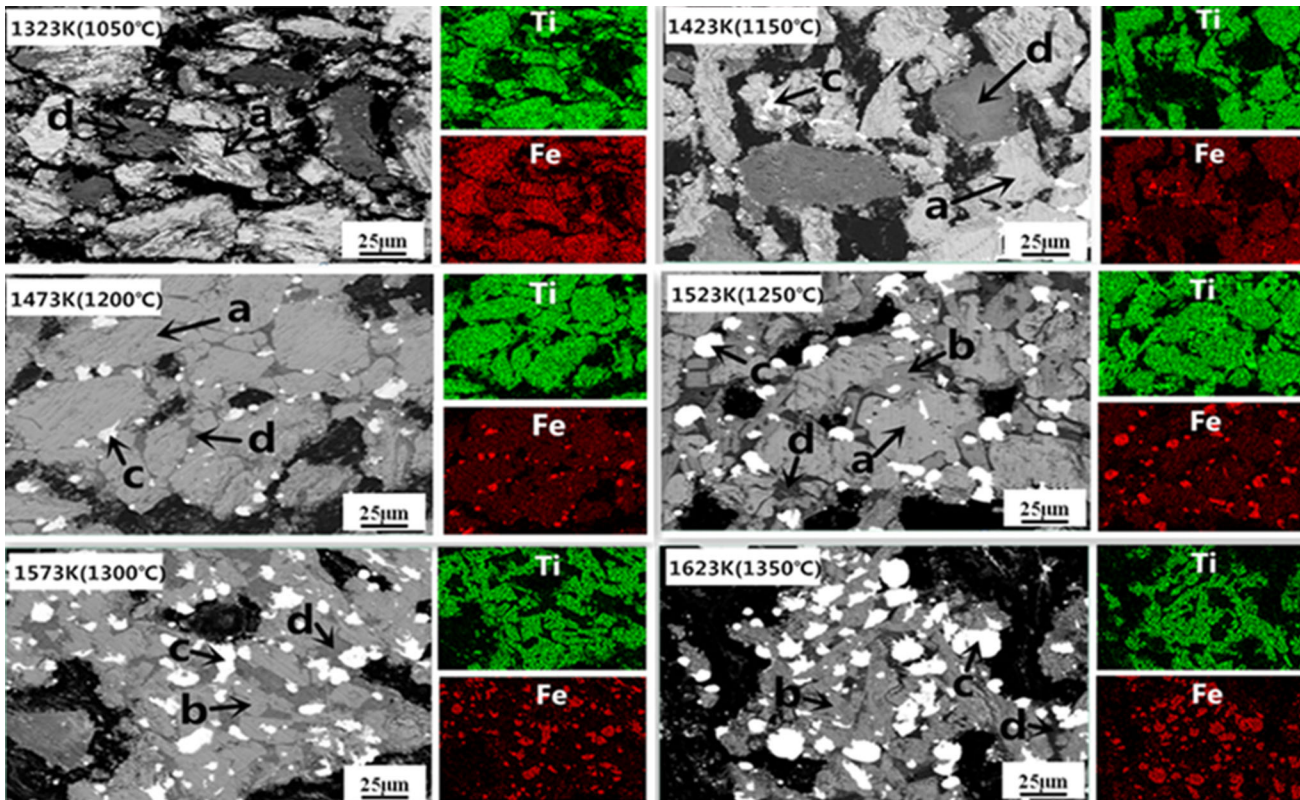


Fig. 6—The morphology and element distribution of the samples reduced with different temperatures: (*a*) titanium-iron oxide (a great quantity of iron), (*b*) titanium-iron oxide (a small amount of iron), (*c*) iron, (*d*) impurity oxide.

Table II. The Average Atomic Percentages of Elements Represented by *a* and *b* (Percent)

	C	O	Mg	Al	Si	S	Ca	Ti	Mn	Fe
1323 K (<i>a</i>)	5.72	58.71	2.34	0.07	0.07	0.01	0.03	16.67	0.31	16.08
1423 K (<i>a</i>)	4.80	57.09	3.73	0.10	0.03	0.03	0.09	18.00	0.33	15.79
1473 K (<i>a</i>)	4.85	57.38	4.00	0.13	0.04	0.01	0.04	18.66	0.36	14.53
1523 K (<i>a</i>)	6.67	56.15	5.89	0.17	0.04	0.02	0.02	18.59	0.58	11.86
1523 K (<i>b</i>)	4.28	59.62	4.70	0.94	0.13	0.00	0.07	24.58	0.16	5.53
1573 K (<i>b</i>)	3.65	59.48	6.46	0.91	0.07	0.00	0.06	27.21	0.30	1.27
1623 K (<i>b</i>)	4.93	58.08	3.70	1.13	0.06	0.03	0.05	30.69	0.05	0.38

Table III. The Average Atomic Percentages of Elements Represented by *c* (Percent)

	C	O	Mg	Al	Si	S	Ca	Ti	Mn	Fe
1473 K (<i>c</i>)	8.27	1.39	0.18	0.00	0.12	0.02	0.11	1.63	0.30	87.98
1523 K (<i>c</i>)	8.60	2.17	0.00	0.25	0.06	0.01	0.02	1.55	0.08	87.26
1573 K (<i>c</i>)	7.77	2.79	0.00	0.02	0.14	0.00	0.17	1.30	0.03	87.78
1623 K (<i>c</i>)	7.84	1.26	0.00	0.09	2.04	0.03	0.00	1.33	0.18	87.23

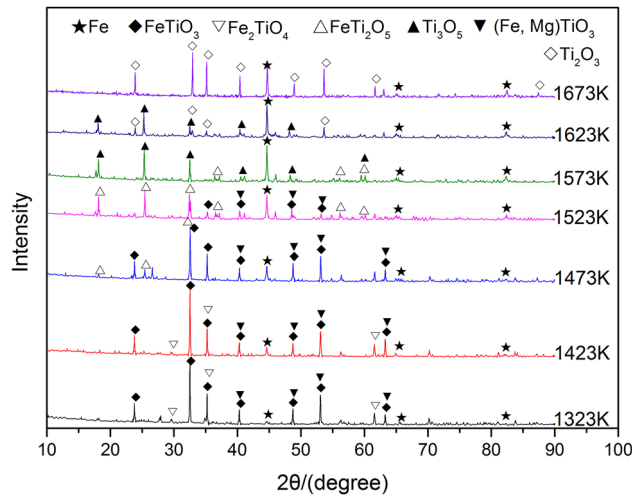


Fig. 7—XRD patterns of product reduced at different temperatures.

Table IV. The Main Phase at Different Temperatures of *a*, *b*, and *c* Contrast

Temperature (K)	Main Phase
1323	Fe, FeTiO ₃ , Fe ₂ TiO ₄ , (Fe,Mg)TiO ₃ , C
1423	Fe, FeTiO ₃ , Fe ₂ TiO ₄ , (Fe,Mg)TiO ₃ , C
1473	Fe, FeTiO ₃ , FeTi ₂ O ₅ , (Fe,Mg)TiO ₃ , C
1523	Fe, FeTiO ₃ , FeTi ₂ O ₅ , (Fe,Mg)TiO ₃ , C
1573	Fe, FeTi ₂ O ₅ , Ti ₃ O ₅ , C
1623	Fe, Ti ₃ O ₅ , Ti ₂ O ₃ , C
1673	Fe, Ti ₂ O ₃ , C

disappeared, and the phase peak of Ti₃O₅ appeared. At 1623 K (1350 °C), the phase peak of FeTi₂O₅ disappeared, the phase peak of Ti₃O₅ weakened, and the phase peaks of Ti₂O₃ appeared. At 1673 K (1400 °C), the phase peak of Ti₃O₅ disappeared, and the phase peak of Ti₂O₃ increased.

The foregoing analysis implied that the type minerals of (Fe, Mg)TiO₃ were presented in the areas of *a*. In the reduction process, iron was gradually reduced and tied up by magnesium to stabilize ilmenite,^[16] which weakened the reduction effect. The iron and magnesium in the areas of *b* decreased at the same time, which indicated that magnesium also began to be reduced with increasing temperature.^[19]

The diagrams of the reduction processes of iron and titanium concentrate based on the foregoing analysis are shown in Figure 8. During the initial reduction, iron was mainly obtained by carbothermal reduction of a small amount of Fe₃O₄ in the sample and by carbothermal reduction of FeTiO₃ and FeTi₂O₅ with increasing temperature.

B. Kinetic Analysis of Reduction Process

For constant heating rate non-isothermal conditions, the reaction rate for a heterogeneous reaction can be described by the following general equation^[23,31–33]:

$$\frac{dx}{dt} = \beta \frac{d\alpha}{dT} = A \exp\left(\frac{-E}{RT}\right) f(\alpha), \quad [1]$$

where *t* is the time, β is the heating rate and $\beta = dT/dt = \text{constant}$, *T* is the temperature, *A* is the pre-exponential factor, *R* is the gas constant, *E* is the activation energy, and *f*(α) is the differential conversion function. By rearranging and integrating Eq. [1], the integral form of mechanism function (*G*(α)) can be obtained:

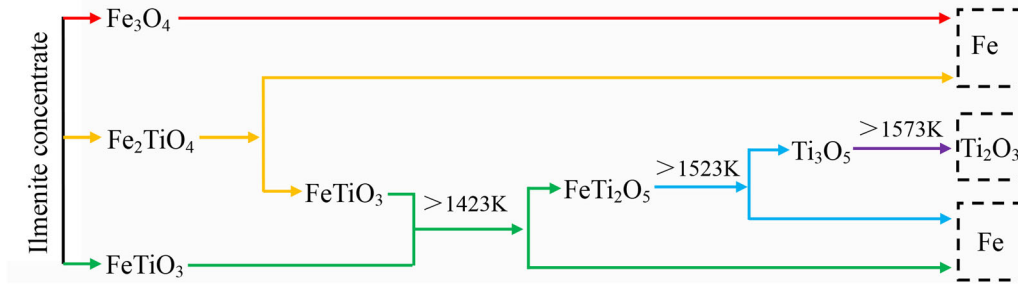


Fig. 8—Reduction process map of iron.

$$G(\alpha) = \int_0^\alpha \frac{d\alpha}{f(\alpha)} = \frac{A}{\beta} \int_{T_0}^T \exp\left(\frac{-E}{RT}\right) dT, \quad [2]$$

$$T = T_0 + \beta t \quad [3]$$

where T_0 is the initial temperature.

In order to determine the most probable mechanism function ($G(\alpha)$), Šatava–Šesták^[34] integral method and Coats–Redfern^[35] integral method were employed on the basis of the metallization ratio of the reduced sample:

$$\begin{aligned} \lg G(\alpha) &= \lg\left(\frac{AE}{R\beta}\right) - 2.315 \\ &- 0.4567 \frac{E}{RT} \text{ (Šatava–Šesták method)}. \end{aligned}$$

The kinetic parameter is calculated from the linear least-squares plot of $\lg G(\alpha)$ vs $1/T$.

$$\begin{aligned} \ln\left(\frac{G(\alpha)}{T^2}\right) &= \ln\left[\frac{AR}{\beta E} \left(1 - \frac{2RT}{E}\right)\right] \\ &- \frac{E}{RT} \text{ (Coats–Redfern method)}. \end{aligned}$$

The kinetic parameter is calculated from the linear least-squares plot of $\ln(G(\alpha)/T^2)$ vs $1/T$.

The integral expressions of mechanism functions used in this work are listed in Table V.

Šatava–Šesták method and Coats–Redfern method were used for linear fitting of mechanism function of Table V, and the same integral function with higher fitting degree in the two methods was chosen as the mechanism function by comparing the fitting results of the two methods, as shown in Table VI and Figure 9. The kinetic mechanism was established by mutual verification of the two methods, and the kinetic parameter of the reduction process calculated by the two methods is shown in Table VII. Therefore, the integral mechanism function that conforms to the condition was $G(\alpha) = [(1-\alpha)^{-1/3}-1]^2$ in the two methods, and the differential for the mechanism function was $f(\alpha) = 3/2(1-\alpha)^{4/3}[(1-\alpha)^{-1/3}-1]^{-1}$. The apparent activation

Table V. Integral Expressions of Common Reaction Mechanism Functions^[33,36,37]

Reaction Model	Integral $G(\alpha)$
1D Diffusion	α^2
2D Diffusion (Valensi)	$\alpha + (1-\alpha)\ln(1-\alpha)$
3D Diffusion (G-B)	$(1-2/3\alpha) - (1-\alpha)^{2/3}$
3D Diffusion (Jander)	$[1 - (1-\alpha)^{1/3}]^n$ ($n = 1/2, 2$)
2D Diffusion (Jander)	$[1 - (1-\alpha)^{1/2}]^{1/2}$
3D Diffusion (Anti-Jander)	$[(1+\alpha)^{1/3}-1]^2$
Avrami-Erofeev	$-\ln(1-\alpha)$
3D Diffusion (Z-L-T)	$[(1-\alpha)^{-1/3}-1]^2$
Avrami-Erofeev	$[-\ln(1-\alpha)]^n$ ($n = 1/4, 1/3, 1/2, 2/3, 2, 3, 4$)
Shrinking Core Model	$1 - (1-\alpha)^n$ ($n = 1/4, 1/3, 1/2, 2, 3, 4$)
Mampel Power Law	α^n ($n = 1/4, 1/3, 1/2, 1, 3/2$)
Chemical Reaction	$(1-\alpha)^{-1}$
Chemical Reaction	$(1-\alpha)^{-1} - 1$
Chemical Reaction	$(1-\alpha)^{-1/2}$

energy of the reduction process was 587.4 ± 2.98 kJ/mol based on the activation energy calculated by the two methods.

C. Analysis of Reduction Mechanism of Iron in Ilmenite Concentrate

Figure 10 shows the reduction mechanism of iron in ilmenite concentrate. In the early stages of reduction, the reductant carbon reacted with the outer layer of the titanium-iron oxide areas, which directly contacted with the areas of a , and the formed product layer (FeTi_2O_5) and a small amount of iron were distributed in the sample. In the middle of reduction, the product of the previous stage (FeTi_2O_5) became a reactant. With the increase of reduction temperature, after the reduction of iron from the outer region of the areas represented by a and b , the iron steaded onto the lining edges of the areas represented by a and b , resulting in the nucleation, aggregation, and growth of iron. In the late stage of

Table VI. Integral and Differential Expressions of Reaction Mechanism Functions

Reaction Model	$G(a)$ (Integral Mechanism Function)	$f(a)$ (Differential Mechanism Function)
3-D Diffusion (Z-L-T)	$[(1-a)^{-1/3}-1]^2$	$3/2(1-a)^{4/3}[(1-a)^{-1/3}-1]^{-1}$

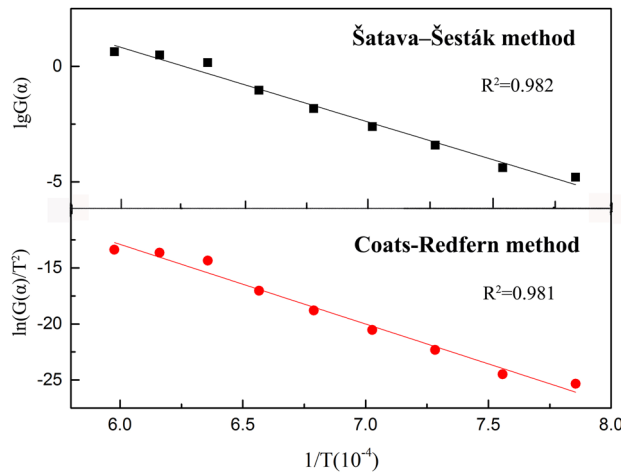


Fig. 9—The mechanism function at Šatava-Šesták method and Coats-Redfern method.

reduction, the iron basically completed the nucleation, aggregation, and growth; the iron particles that had already grown did not move and would continue to grow by receiving the diffused iron around it and result in the coarsening of iron. When the grown iron, which

was very close to each other, continued to grow to a certain extent, it combined to become a larger iron particle.

V. CONCLUSIONS

The non-isothermal reduction kinetics and mechanism of iron during vacuum carbothermal reduction of ilmenite concentrate were investigated by X-ray diffraction, backscattered electron imaging, and energy-dispersive X-ray spectroscopy at temperatures from 1273 K to 1673 K (1000 °C to 1400 °C). The following conclusions are obtained:

- (1) The increasing trends of mass loss ratio, metallization ratio, and pressure were similar to the increase in temperature at 1273 K to 1573 K (1000 °C to 1300 °C). When the temperature was higher than 1573 K (1300 °C), the pressure decreased, and the increasing trends of metallization and mass loss ratios slowed down. At 1673 K (1400 °C), the metallization ratio reached up to 94.3 pct, and the iron reduction was close to completion.
- (2) The XRD and EDS results indicated that iron was mainly obtained by carbothermal reduction of FeTiO_3 and FeTi_2O_5 . A small amount of Fe_2TiO_4 was

Table VII. Kinetic Parameter of the Reduction Process Calculated by the Two Methods

	Coats-Redfern Method	Šatava-Šesták Method	Average
Apparent Activation Energy E (kJ/mol)	590.4	584.4	587.4
Pre-exponential A (s^{-1})	3.39×10^{18}	2.21×10^{18}	2.80×10^{18}

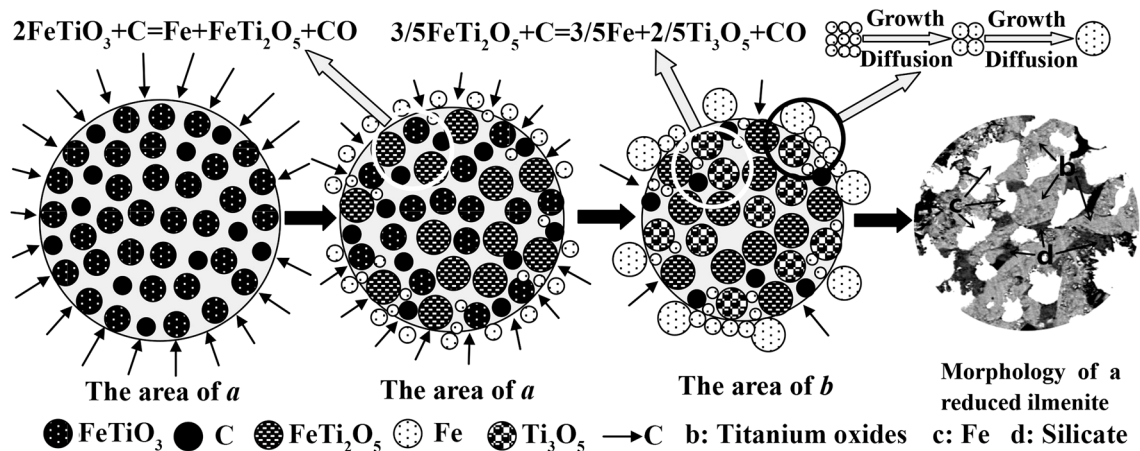


Fig. 10—Reduction mechanism diagram of ilmenite concentrate.

produced in the early stage of reduction, the reaction products were iron and Ti_2O_3 .

- (3) During the reduction process, iron diffused out of the product layer and then steadied onto the junction between the aggregation region of titanium-iron oxide and the aggregation region of silicate compounds. With increasing reduction temperature, the iron became larger by continuous nucleation, aggregation, and growth.
- (4) Comprehensive consideration of Šatava–Šesták method and Coats–Redfern method, the apparent activation energy of the reduction process was 587.4 ± 2.98 kJ/mol, and the forms of both integral and differential for the mechanism function were $G(a) = [(1-a)^{-1/3}-1]^2$ and $f(a) = 3/2(1-a)^{4/3}[(1-a)^{-1/3}-1]^{-1}$, respectively.

ACKNOWLEDGMENTS

The authors are especially grateful for the financial support from the National Natural Science Fund of China (No. 51404080, No. 51664003). The chemical compositions of all the samples were analyzed by Panzhihua Iron & Steel Research Institute, Pan Gang Group.

REFERENCES

1. D.C. Li, D.L. Zhou, and H. Liu: *Sponge Titanium Production of Magnesiothermy*, 1st ed., Metallurgical Industry Press, Beijing, 2009, pp. 5–6.
2. W. Mo, G.Z. Deng, and F.C. Luo: *Titanium Metallurgy*, 2nd ed., Metallurgical Industry Press, Beijing, 1998, p. 124.
3. G.Z. Deng: *Titanium Metallurgy*, 1st ed., Metallurgical Industry Press, Beijing, 2010, p. 55.
4. S.S. Liu, Y.F. Guo, G.Z. Qiu, T. Jiang, and F. Chen: *Trans. Nonferr. Met. Soc. China (English Edition)*, 2013, vol. 23, pp. 1174–78.
5. X. Wu, J.B. Zhang, H.J. Miao, E.D. Ye, and X.Y. Zhang: *Iron Steel Vanadium Titanium*, 2016, vol. 37, pp. 1–7.
6. Y.F. Guo, S.S. Liu, X.W. Ma, T. Jiang, and G.Z. Qiu: *Trans. Nonferr. Met. Soc. China*, 2010, vol. 20, pp. 2038–44.
7. R. Huang, X.W. Lv, C.G. Bai, Q.Y. Deng, and S.W. Ma: *Can. Metall. Q.*, 2013, vol. 51, pp. 434–39.
8. B.B. Shao, W.Z. Ding, D.S. Tan, X.F. Shang, and S.Q. Guo: *Hydrometall. China*, 2018, vol. 37, pp. 14–19.
9. W. Lv, C.G. Bai, X.W. Lv, K. Hu, X.M. Lv, J.Y. Xiang, and B. Song: *Powder Technol.*, 2018, vol. 340, pp. 354–61.
10. K. Zhang, X.W. Lv, R. Huang, B. Song, and F. Xi: *Metall. Trans. B.*, 2014, vol. 45, pp. 923–28.

11. M.A.R. Dewan, G. Zhang, and O. Ostrovski: *ISIJ Int.*, 2010, vol. 50, pp. 647–53.
12. J.L. Li, B. Ma, Q.G. Yan, Y.F. Zhu, and K.J. Reid: *Eng. Chem. Metall.*, 1990, vol. 21, pp. 225–30.
13. N.J. Welham and J.S. Williams: *Metall. Trans. B.*, 1999, vol. 30, pp. 1075–81.
14. H.P. Gou, G.H. Zhang, X.J. Hu, and G.Z. Zhou: *Trans. Nonferr. Met. Soc. China (English Edition)*, 2017, vol. 27, pp. 1856–61.
15. W. Lv, X.W. Lv, J.Y. Xiang, J.S. Wang, X.M. Lv, C.G. Bai, and B. Song: *Int. J. Miner. Process.*, 2017, vol. 169, pp. 176–84.
16. Y. Wang and Z. Yuan: *Int. J. Min. Pro.*, 2006, vol. 81, pp. 133–40.
17. M.I. El-Guindy and W.G. Davenport: *Metall. Trans.*, 1970, vol. 1, pp. 1729–34.
18. Y.N. Dai and B. Yang: *Vacuum Metallurgy of Nonferrous Metals*, 2nd ed., Metallurgical Industry Press, Beijing, 2009, pp. 1–3.
19. R. Huang, P.S. Liu, X. Qian, and J.Z. Zhang: *Vacuum*, 2016, vol. 134, pp. 20–24.
20. R. Huang, P.S. Liu, J.Z. Zhang, and Y.H. Yue: *Metallurgist*, 2017, vol. 61, pp. 511–16.
21. R. Huang, P.S. Liu, Y.H. Yue, and J.Z. Zhang: *Miner. Process. Extr. Metall. Rev.*, 2017, vol. 38, pp. 193–98.
22. M.J. Hu, R.R. Wei, M.L. Hu, L.Y. Wen, and F.Q. Ying: *JOM.*, 2018, vol. 70, pp. 1443–48.
23. Y.S. Sun, Y.X. Han, X.C. Wei, and P. Gao: *J. Therm. Anal. Calorim.*, 2016, vol. 123, pp. 703–15.
24. X.M. Lv, W. Lv, Z.X. You, X.W. Lv, and C.G. Bai: *Powder Technol.*, 2018, vol. 340, pp. 495–501.
25. M.H. El-Sadek, H.M. Ahmed, K. El-Barawy, M.B. Morsi, H. El-Didamony, and B. Björkman: *J. Therm. Anal. Calorim.*, 2017, vol. 1, pp. 1–9.
26. Y.R. Liu, J.L. Zhang, X.D. Xing, Z.J. Liu, X.L. Liu, N.Y. Li, and Y.S. Shen: *Metall. Mater. Trans. B.*, 2017, vol. 48B, pp. 2419–27.
27. Y.H. Yue: *Experimental study on Vacuum Carbon Thermal Reduction of Ilmenite Concentrate*, Guizhou University, GuiYang, 2016, pp. 63–64.
28. C.W. Li, X.G. Si, X.G. Lu, S.Q. Guo, and W.Z. Ding: *Metall. Anal.*, 2011, vol. 31, pp. 40–44.
29. X. Fu, Y. Wang, and F. Wei: *Metall. Trans. A.*, 2010, vol. 41, pp. 1338–48.
30. T. Hu, X.W. Lv, C.G. Bai, Z. Lun, and G. Qiu: *Metall. Trans. B.*, 2013, vol. 44, pp. 252–60.
31. M.X. Huang, C.R. Zhou, and X.W. Han: *J. Therm. Anal. Calorim.*, 2013, vol. 113, pp. 589–93.
32. M. Otero, L.F. Calvo, M.V. Gil, A.I. Garcia, and A. Morán: *Bioresour. Technol.*, 2008, vol. 99, pp. 6311–19.
33. R.Z. Hu, S.L. Gao, F.Q. Zhao, Q.Z. Shi, T.L. Zhang, and J.J. Zhang: *Kinetics of Thermal Analysis*, 2nd ed., Science Press, Beijing, 2008, pp. 54–55.
34. F. Šatava and J. Šesták: *J. Therm. Anal.*, 1975, vol. 8, pp. 477–89.
35. A.W. Coats and J.P. Redfern: *III. Polym. Sci.*, 1965, vol. 3, pp. 917–20.
36. P. Li, Q.B. Yu, H.Q. Xie, Q. Qin, and K. Wang: *Energ. Fuels*, 2013, vol. 27, pp. 4810–17.
37. P. Li, Q.B. Yu, Q. Qin, and W. Lei: *Ind. Eng. Chem. Res.*, 2012, vol. 51, pp. 15872–83.

Publisher's Note Springer Nature remains neutral with regard to jurisdictional claims in published maps and institutional affiliations.